Research Square

Preprints are preliminary reports that have not undergone peer review.
They should not be considered conclusive, used to inform clinical practice,
or referenced by the media as validated information.

Limit Support Pressure and Critical Cover-to-Diameter Ratio of Shallow-Buried Tunnel Faces in Sand-over- Clay Composite Ground

Kun YANG
Beijing Urban Construction Exploration & Surveying Design Research Institute Co., Ltd
Jian XU
JianXu_ucd@163.com

Beijing Urban Construction Exploration & Surveying Design Research Institute Co., Ltd
Bolin JIANG
Chongqing Jiaotong University
Chen TANG
Beijing Urban Construction Exploration & Surveying Design Research Institute Co., Ltd
Weitong HE
Beijing Urban Construction Exploration & Surveying Design Research Institute Co., Ltd

Research Article

Keywords: shallow-buried tunnel, composite ground, tunnel face stability, limit support pressure, critical cover-to-diameter ratio, lower-bound limit analysis

Posted Date: September 3rd, 2026

DOI: https://doi.org/10.21203/rs.3.rs-10676164/v1

License: This work is licensed under a Creative Commons Attribution 4.0 International License.
Read Full License

Additional Declarations: No competing interests reported.

Limit Support Pressure and Critical Cover-to-Diameter Ratio of Shallow-Buried Tunnel Faces in Sand-over-Clay Composite Ground

Kun YANG[1,2], Jian XU[1,2,*], Bolin JIANG[3], Chen TANG[1,2], Weitong HE[1,2]

(1. Beijing Urban Construction Exploration & Surveying Design Research Institute Co., Ltd., Beijing 100101, China;

2. Beijing Key Laboratory of Deep Foundation Pit Engineering for Urban Rail Transit, Beijing 100101, China;

3. School of Civil Engineering, Chongqing Jiaotong University, Chongqing 400074, China)

*Corresponding Email: jianxu_ucd@163.com

Abstract: To investigate the failure mechanism and stability control conditions of shallow-buried tunnel faces in sand-over-clay composite ground, centrifuge model tests, particle image velocimetry (PIV), and three-dimensional lower-bound finite-element limit analysis were employed to examine the effects of the soil-layer interface position, cover-to-diameter ratio, and internal friction angle of the upper sand layer on the failure mode, earth-pressure release, and limit support pressure. The results show that when the soil-layer interface intersects the center of the tunnel face, face instability is governed primarily by the upper sand layer, with the failure zone propagating upward and outward from the tunnel face. As the cover-to-diameter ratio increases from 0.8 to 1.2, the extent of the affected zone increases, whereas the peak surface settlement decreases from approximately 15 mm to 8 mm. When the soil-layer interface is located at the tunnel crown, the lower clay layer effectively restricts the upward propagation of the failure zone. In this case, the failure zone remains mainly within 1.5 tunnel diameters ahead of the face, and no continuous failure surface is formed even when the face retraction displacement reaches 30 mm. Earth-pressure release in the sand layer is significantly greater than that in the clay layer, and the face retraction process can be divided into three stages: local deformation, progressive failure, and residual stability. The limit support pressures for cases D1 and D2 are 12.7 kPa and 13.4 kPa, respectively. The three-dimensional lower-bound analysis yields deviations of less than 10% from the centrifuge test results and satisfactorily reproduces the failure characteristics of the tunnel face in composite ground. As the internal friction angle of the upper sand layer increases from 15° to 35°, the critical cover-to-diameter ratio decreases from 2.20 to 1.10, while the corresponding critical limit support pressure coefficient decreases from 0.118 to 0.054. An approximately linear relationship is obtained between the critical cover-to-diameter ratio and the internal friction angle, with a coefficient of determination of R^2=0.995. These findings provide a reference for determining tunnel-face support parameters and assessing the risk of global failure in shallow-buried tunnels constructed in sand-over-clay composite ground.

Keywords: shallow-buried tunnel; composite ground; tunnel face stability; limit support pressure; critical cover-to-diameter ratio; lower-bound limit analysis

0 Introduction

With the rapid expansion of urban underground space development and rail transit construction, shallow-buried tunnels are increasingly encountering complex geological conditions. The tunnel face, as the unsupported boundary directly exposed to the unexcavated ground during construction, plays a critical role in construction safety and surface deformation control. For homogeneous sandy ground, Kirsch [1] investigated the failure process of shallow tunnel faces through model tests and demonstrated that sand density has a pronounced influence on the geometry of the failure zone. Chen et al. [2] further revealed the progressive development of tunnel-face failure in sandy ground through three-dimensional model tests. Liu et al. [3], based on large-scale 1g model tests, found that the support pressure decreases

rapidly during face retraction and subsequently tends to stabilize, accompanied by significant ground deformation and surface settlement. Lü et al. [4] further examined tunnel-face stability in sandy ground under seepage conditions and showed that hydraulic conditions can alter both the failure mode and the limit support pressure. In addition to sandy ground, Weng et al. [5] investigated the progressive failure process and limit support pressure of tunnel faces in soft clay through centrifuge tests and numerical simulations. These studies indicate that tunnel-face instability generally exhibits a pronounced progressive evolution, and that the extent of the failure zone and the required support pressure are jointly influenced by soil strength, cover depth, and the stress-release process.

Compared with homogeneous ground, layered or composite ground exhibits greater complexity because of the contrasting strength and deformation characteristics of different soil layers. Berthoz et al. [6] investigated tunnel-face failure in homogeneous and stratified soft ground using 1g reduced-scale tests combined with theoretical analysis, confirming the significant influence of stratification on the failure mechanism. Alagha and Chapman [7] employed three-dimensional finite-element analysis to compare cases in which the soil-layer interface was located at the tunnel crown, at the center of the tunnel face, and at other elevations, and found that both the strength contrast between soil layers and the interface position significantly affect the limit support pressure. For multilayered ground, Ibrahim et al. [8] developed a three-dimensional failure mechanism for multilayered frictional soils, while Senent and Jimenez [9] further considered the possibility of both global and partial failure in layered ground. Han et al. [10] investigated tunnel-face stability in multilayered cohesive-frictional soils using upper-bound limit analysis and demonstrated that the mechanical properties and spatial arrangement of different soil layers have a significant effect on the limit support pressure.

In recent years, experimental and theoretical studies have increasingly focused on complex composite ground characterized by pronounced contrasts in material properties. Ma et al. [11] conducted large-scale transparent-soil model tests to investigate tunnel-face failure in clay and clay–gravel composite ground, revealing the evolution of the failure zone under different ground configurations. Tu et al. [12] studied tunnel-face stability in inclined layered ground using three-dimensional limit analysis and showed that both the spatial position and inclination of the soil-layer interface influence the geometry of the potential failure zone and the critical support pressure. More recently, Li et al. [13] investigated shallow shield tunnels in sand–clay layered ground using centrifuge tests and three-dimensional discrete-element analysis. They systematically examined the effects of interface elevation, dip angle, and cover-to-diameter ratio on the critical support pressure and failure-zone evolution, and found that the position of the sand–clay interface relative to the tunnel face exerts a more pronounced influence on support pressure than the interface inclination. These findings further demonstrate that tunnel-face stability in sand–clay composite ground cannot be adequately evaluated using assumptions developed for homogeneous ground.

In theoretical analyses of tunnel-face stability, conventional limit-equilibrium and upper-bound limit-analysis methods generally require a predefined potential failure mechanism, and their results may therefore depend on the assumed failure pattern. Numerical limit analysis, by contrast, can directly determine admissible stress or velocity fields through finite-element discretization and optimization, providing an alternative approach for identifying nonuniform failure zones in complex ground. Fernández et al. [14] investigated the stability of shallow tunnel faces using three-dimensional numerical limit analysis and the material point method, and showed that lower-bound numerical limit analysis can effectively predict the minimum support pressure and global failure mechanism of the tunnel face. This provides a theoretical basis for analyzing shallow tunnel-face instability through statically admissible

stress fields.

Although the above studies have established a solid basis for tunnel-face stability analysis in layered and composite ground, several issues remain to be further investigated for shallow-buried tunnels in sand-over-clay composite ground. First, existing studies on sand–clay composite ground have begun to address the effects of interface position, inclination, and cover depth [14], but systematic comparisons of deformation differences between sand and clay, earth-pressure release, and the progressive failure process remain limited when the horizontal soil-layer interface is located at either the center of the tunnel face or the tunnel crown. Second, previous model tests have mainly focused on failure morphology and limit support pressure, whereas the relationships among support-stress degradation, earth-pressure release, and displacement-field evolution have received comparatively less attention. Third, when the shear strength of the upper sand layer and the cover depth vary simultaneously, a quantitative criterion is still lacking for the critical cover-to-diameter ratio at which the potential failure zone changes from a global failure mechanism extending to the ground surface to a locally confined failure mechanism ahead of the tunnel face. Existing limit-analysis studies on layered ground have shown that both strength contrast and interface position can significantly alter the failure mode [8–10,12], indicating the need for further investigation of both the failure process and the critical transition condition in sand-over-clay composite ground.

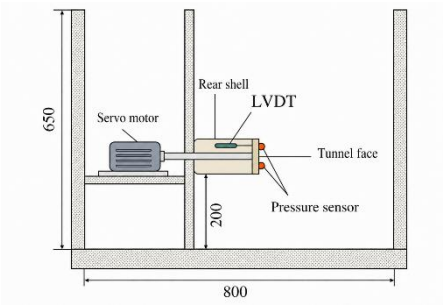
Accordingly, this study employs centrifuge model tests, particle image velocimetry (PIV), and three-dimensional lower-bound finite-element limit analysis to investigate the stability of shallow-buried tunnel faces in sand-over-clay composite ground. By varying the soil-layer interface position and the cover-to-diameter ratio, the evolution of the displacement field, earth-pressure release, and support pressure during face retraction is examined, and the progressive failure stages and limit state are identified. On the basis of the experimental results, the three-dimensional lower-bound limit-analysis method is then used to identify the potential yielded zone and corresponding failure mode. Furthermore, the combined effects of the internal friction angle of the upper sand layer and the cover-to-diameter ratio are investigated to determine the critical cover-to-diameter ratio associated with the transition from global failure to local failure. The results are intended to provide a reference for determining tunnel-face support parameters and assessing global failure risk in shallow-buried tunnels constructed in similar composite ground conditions.

1 Centrifuge Model Test Program

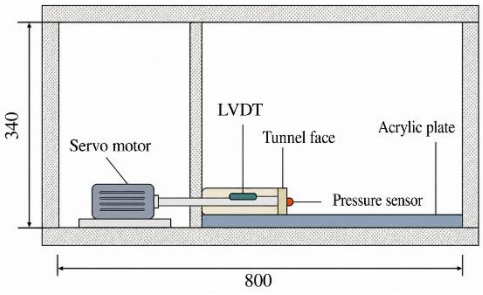
1.1 Test Apparatus and Materials

The tests were conducted using a TLJ-3 geotechnical centrifuge at Chang'an University. The centrifuge has a maximum capacity of 60 g·t, a maximum centrifugal acceleration of 200g, and a rotational radius of 2 m. The model tunnel had a diameter of 100 mm, corresponding to a prototype diameter of 6 m at a geometric scale of 1:60, and the centrifugal acceleration was set to 60g during the tests. The experimental apparatus is shown in Fig. 1. The internal dimensions of the model box were 800 mm × 340 mm × 650 mm (length × width × height).

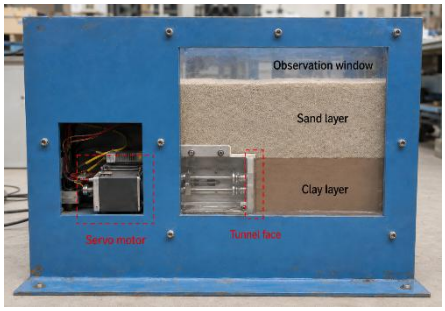
ISO standard sand was used for the sand layer, while the clay was collected from an engineering project and subsequently subjected to impurity removal, air drying, and sieving. The material properties are listed in Table 1.



(a) Front-view schematic



(b) Plan-view schematic



(c) Model box

Fig. 1 Experimental apparatus

Table 1 Soil properties

Soil layer	Density /(g·cm⁻³)	Internal friction angle /(°)	Cohesion /kPa	Compression modulus /MPa	Poisson's ratio
Sand	1.62	28	0	25	0.27
Clay	1.30	24	15	15	0.33

1.2 Test Conditions and Monitoring Scheme

Four test cases were designed. In cases D1 and D2, the soil-layer interface intersected the center of the tunnel face, whereas in cases D3 and D4, the interface was located at the tunnel crown. The cover-to-diameter ratio *C*/*D* was set to 0.8 for D1 and D3 and 1.2 for D2 and D4, as summarized in Table 2. The model configuration and soil-layer interface are illustrated in Fig. 2.

Table 2 Test conditions

Case	*C*/*D*	Position of soil-layer interface	Maximum face retraction displacement / mm
D1	0.8	Center of tunnel face	30
D2	1.2	Center of tunnel face	30
D3	0.8	Tunnel crown	30
D4	1.2	Tunnel crown	30

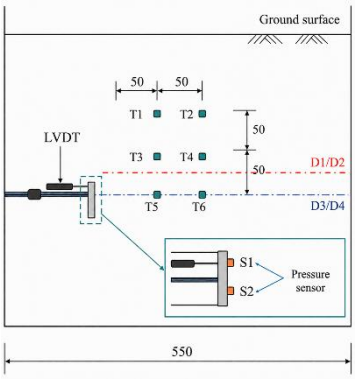


Fig. 2 Soil-layer interface and monitoring layout

The monitoring layout is shown in Fig. 2. During the tests, a laser displacement sensor was used to measure the face retraction displacement, while a motion camera continuously recorded the soil deformation for subsequent particle image velocimetry (PIV) analysis of the displacement field. One earth pressure cell was installed at each of the upper (S1) and lower (S2) central positions of the tunnel face plate, and six additional earth pressure cells were embedded in the soil ahead of the tunnel face at different depths.

1.3 Test Procedure

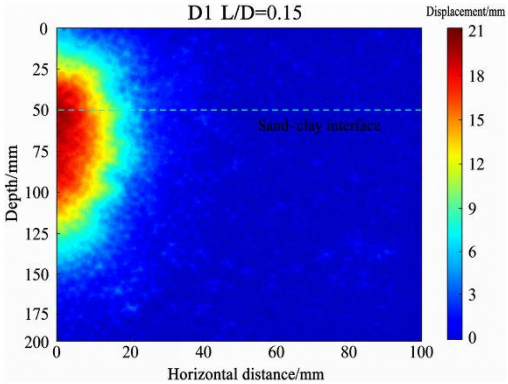
The test procedure was as follows: (1) The model box was mounted on the centrifuge basket, and the centrifuge was started. The centrifugal acceleration was gradually increased to 60g and maintained for 25 min to establish a stable stress field, during which the initial sensor readings were recorded. (2) After the measured data stabilized, the stepper motor was activated remotely to retract the tunnel face at a constant rate of 0.5 mm/s. The prescribed total face retraction displacement was 30 mm, corresponding to a retraction duration of 60 s. The calculated ratio of inertial force to static force satisfied the requirements for quasi-static loading. (3) During face retraction, the face displacement, support force, and earth pressure were continuously recorded, while a motion camera continuously captured images of soil deformation. When the prescribed retraction displacement was reached and the support force became stable, the motor was stopped. (4) The centrifugal acceleration was then gradually reduced to zero. After the centrifuge had completely stopped, the model box was removed, cleaned, and prepared for the subsequent test.

2 Test Results and Analysis

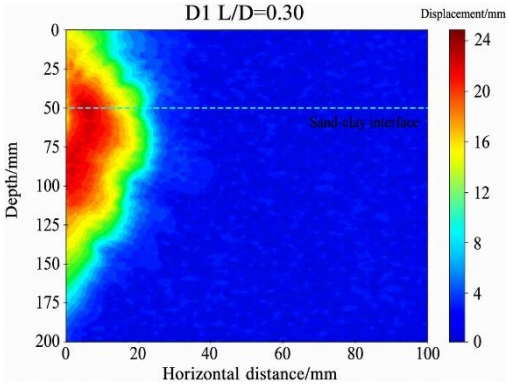
2.1 Displacement Characteristics of the Failure Zone

A motion camera was used to continuously record soil deformation during tunnel-face retraction, and the captured images were processed using particle image velocimetry (PIV) to obtain the displacement fields of the soil ahead of the tunnel face under different test conditions, as shown in Fig. 3. At L/D=0.15, the high-displacement zone (red region) in case D1 had already extended to the ground surface (i.e., 0 mm below the surface), whereas that in case D2 remained confined to the middle and lower portions of the sand layer. This indicates that the ground-surface response to excavation-induced disturbance was more rapid under the smaller cover-to-diameter ratio. When L/D increased to 0.30, the failure zone in D1 widened considerably, with the high-displacement region expanding laterally. In contrast, the displacement zone in D2 extended markedly downward, reaching a depth of more than 150 mm, while its horizontal extent also exceeded that observed in D1. For both cases, the maximum displacement occurred in the middle-to-upper portion of the sand layer and gradually migrated upward with increasing face retraction, indicating that the excavation-induced disturbance propagated upward

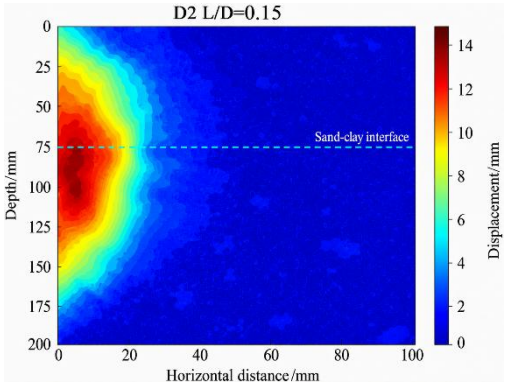
from the vicinity of the tunnel face into the overlying soil.



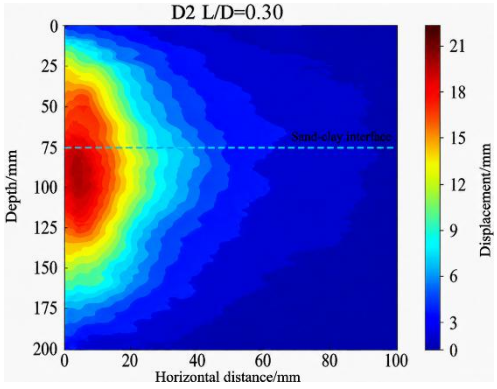
(a) D1 *L*/*D*=0.15



(b) D1 *L*/*D*=0.30



(c) D2 *L*/*D*=0.15



(d) D2 *L*/*D*=0.30

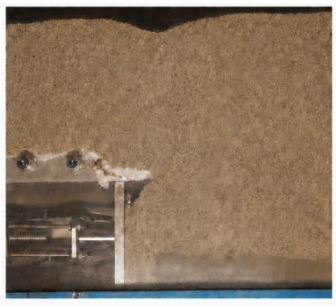
Fig. 3 Comparison of displacement fields ahead of the tunnel face for cases D1 and D2

2.2 Characteristics of the Final Failure-Zone Profile

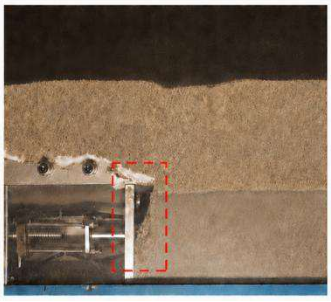
A comparison of the final failure-zone profiles and surface settlement troughs for cases D1 and D2 (Fig. 4) shows that the failure zone in D1 exhibited a narrow upper portion and a wider lower portion, with its upper boundary extending to the ground surface. The surface settlement trough displayed a relatively high and narrow single-peak profile, with a maximum settlement of approximately 15 mm directly above the tunnel centerline. In addition, almost the entire sand layer above the sand–clay interface was involved in the failure zone. In case D2, the failure zone was more extensive, whereas the surface settlement trough was noticeably broader and flatter, with a maximum settlement of approximately 8 mm. Meanwhile, the lower portion of the sand layer remained relatively intact.



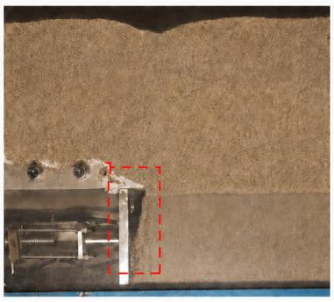
(a) D1



(b) D2



(c) D3



(d) D4

Fig. 4 Final deformation under different test conditions

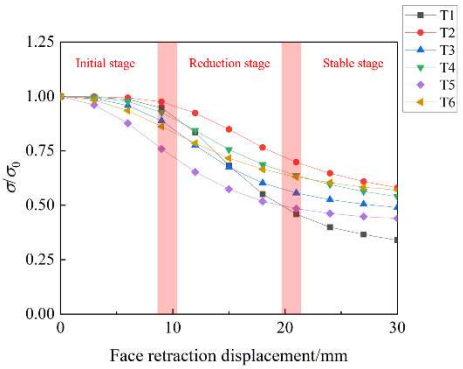
2.3 Variation in Earth Pressure

As the face retraction displacement increased, the vertical earth pressure at all monitoring points decreased to varying degrees. In case D1, the final stress release ratio reached 66% at monitoring point T1 in the sand layer, compared with only 56% at T5 in the clay layer, indicating that the sand layer was more sensitive to unloading induced by face retraction. When the cover-to-diameter ratio increased, as in case D2, the stress release ratios at all monitoring points except T1 decreased by 6–40 percentage points relative to those in D1, indicating an overall reduction in earth-pressure release at most monitoring locations as the cover depth increased. The higher stress release at T1 in D2 is attributed to local stress redistribution caused by the wider and deeper disturbed zone.

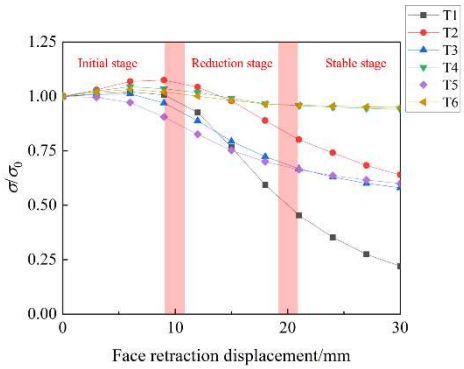
When the soil-layer interface was located at the tunnel crown (D3 and D4), the entire tunnel face was situated within the clay layer. The maximum stress release ratio was less than 12%, and the reduction in earth pressure occurred mainly during the initial stage of face retraction, after which the earth pressure gradually stabilized. Along the depth direction, the shallow monitoring points (T1 and T2) responded earlier than the deeper points (T5 and T6), indicating an upward propagation of the disturbance. The final stress release ratios at representative monitoring points for all test cases are summarized in Table 3.

Table 3 Final stress release ratios at representative monitoring points for different test cases (%)

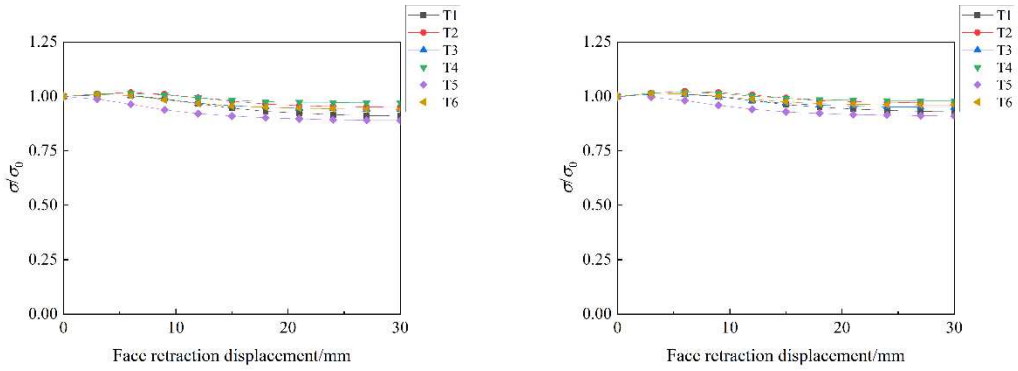
Case	T1	T2	T3	T4	T5	T6
D1	66	42	51	46	56	43
D2	78	36	42	6	40	5
D3	9	5	6	3	11	6
D4	7	3	5	2	9	4



(a) D1



(b) D2



(c) D3 (d) D4

Fig. 5 Normalized vertical earth pressure versus face retraction displacement

2.4 Tunnel-Face Support pressure Characteristics

The tunnel-face support pressure ratio was defined as $\lambda=P_s/P_0$,where P_s is the measured support pressure and P_0 is the initial support pressure. The variation in λ with normalized face retraction L/D exhibited three distinct stages: (1) a rapid reduction stage at L/D <0.2%; (2) a gradual reduction stage at 0.2%≤L/D<10%; and (3) a stable stage at L/D≥10%. For the failure cases D1 and D2, the support pressure ratio at the upper center of the tunnel face, corresponding to the sand layer, consistently decreased faster than that at the lower center in the clay layer and reached the limit state first. No abrupt reduction was observed at the lower central point throughout the face retraction process.

Table 4 summarizes the characteristic parameters of tunnel-face support pressure for all test cases. The limit support pressure ratios for D1 and D2 were 0.21 and 0.19, respectively, corresponding to limit support pressures of 12.7 kPa and 13.4 kPa. As the cover-to-diameter ratio increased from 0.8 to 1.2, the limit support pressure increased from 12.7 kPa to 13.4 kPa, corresponding to an increase of only 5.5%. This indicates that, for the cases in which the soil-layer interface intersected the center of the tunnel face, the limit support pressure was relatively insensitive to the variation in cover-to-diameter ratio within the investigated range. For cases D3 and D4, the support pressure ratio remained above 0.85 throughout the tests, and no failure characteristics were observed.

Table 4 Characteristic parameters of tunnel-face support pressure

Case	**Position of soil-layer interface**	***C*/*D***	**Limit λ_{min} at upper center**	**Limit λ_{min} at lower center**	**Limit support pressure P_{min} / kPa**
D1	Center of tunnel face	0.8	0.21	0.35	12.7
D2	Center of tunnel face	1.2	0.19	0.31	13.4
D3	Tunnel crown	0.8	—	—	—
D4	Tunnel crown	1.2	—	—	—

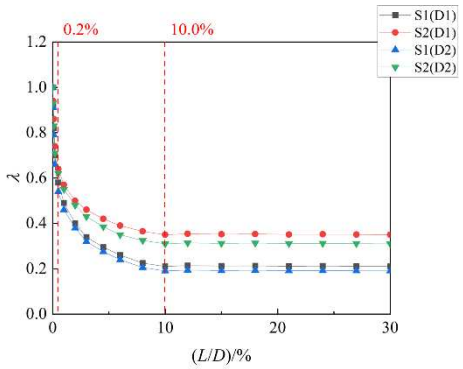


Fig. 6 Face retraction–support pressure ratio curves

2.5 Identification of Tunnel-Face Failure Stages

Based on the support pressure ratio curves, PIV displacement fields, and vertical earth-pressure responses, the tunnel-face retraction process can be divided into three stages. In the initial stage, soil deformation was concentrated primarily in the vicinity of the tunnel face and the affected zone remained limited, corresponding to the local deformation stage. Subsequently, the displacement zone gradually propagated upward and outward, accompanied by continuous earth-pressure release, indicating the progressive failure stage. Once the support pressure ratio approached a stable plateau and a continuous displacement band had essentially developed, the system entered the residual stability stage.

The transition point at which the support pressure ratio curve first entered the stable plateau was adopted as the criterion for identifying the limit state. This criterion was verified by the formation of a continuous failure zone in the PIV displacement field, while the pronounced release of vertical earth pressure was used as a supplementary indicator. Cases D1 and D2 both reached the limit state at a face retraction displacement of approximately 10 mm, as summarized in Table 5.

Table 5 Limit states obtained from the centrifuge tests

Case	Limit face retraction displacement / mm	Limit support pressure ratio at S1	Limit support pressure ratio at S2	Limit support pressure / kPa
D1	10	0.21	0.35	12.7
D2	10	0.19	0.31	13.4

After D1 and D2 reached the limit state, only minor fluctuations were observed in the support pressure ratio, indicating that the tunnel face had transitioned from progressive failure to the residual stability stage. For D3 and D4, no continuous failure zone developed in the displacement field within the prescribed face retraction range of 30 mm, and only minor variations in vertical earth pressure were recorded. Therefore, these two cases were considered not to have reached the limit state within the test range.

3 Three-Dimensional Lower-Bound Limit Analysis

A three-dimensional lower-bound finite-element limit analysis method was employed to determine the limit support pressure of the tunnel face in sand-over-clay composite ground and to investigate the effects of the cover-to-diameter ratio and soil-layer interface position on face stability. Based on the lower-bound theorem of limit analysis, the method determines the minimum support pressure required to maintain tunnel-face stability by constructing a statically admissible stress field that simultaneously satisfies static equilibrium, stress boundary conditions, and the material yield criterion.

3.1 Basic Principles

The stress field at any point within the computational domain should satisfy the static equilibrium

condition:

$$\nabla \cdot \sigma + b = 0 \tag{1}$$

where σ is the stress tensor and b is the body force induced by the self-weight of the soil.

On the stress boundary, the following condition should be satisfied:

$$\sigma n = \bar{t} \tag{2}$$

where n is the outward unit normal vector to the boundary and $\bar{t}$ is the prescribed boundary traction.

The Mohr–Coulomb yield criterion was adopted for both the upper sand layer and the lower clay layer. Based on the transformation method proposed by Krabbenhoft et al. [15], with auxiliary matrix variables introduced and compressive stress taken as positive, the yield condition can be expressed as:

$$f(\sigma) = (1-\sin\phi)\sigma_1 - (1+\sin\phi)\sigma_3 - 2c\cos\phi \le 0 \tag{3}$$

where σ_1 and σ_3 are the major and minor principal stresses, respectively; c and ϕ are the cohesion and internal friction angle of the soil, respectively. Continuity of both the normal and shear stresses was imposed across the soil-layer interface.

3.2 Computational Model and Boundary Conditions

The computational model consisted of the soil mass ahead of the tunnel face, the overlying ground, and the tunnel excavation region. As shown in Fig. 7, the model dimensions were 30 m in width (B), 25 m in height (H_g), and 20 m in longitudinal length (L). The tunnel diameter D was 6 m, and the cover depth C, measured from the tunnel crown to the ground surface, was 4.8 and 7.2 m, corresponding to C/D=0.8 and 1.2. The soil parameters were consistent with those adopted in the centrifuge tests (Table 1).

The ground surface and unsupported excavation boundaries were treated as free boundaries, while a uniformly distributed normal support pressure was applied to the tunnel face. The lateral and bottom boundaries of the computational domain were positioned sufficiently far from the tunnel face, and their normal displacements were constrained to minimize boundary effects. Continuous contact was assumed between the upper and lower soil layers, with no interface separation or relative sliding considered.

The computational domain was discretized using four-node tetrahedral elements. The stress field within each element was approximated using piecewise interpolation, with element equilibrium conditions, stress continuity across common faces of adjacent elements, and the Mohr–Coulomb yield constraints imposed simultaneously. Local mesh refinement was adopted near the tunnel face, soil-layer interface, and potential failure zone to improve the computational accuracy of the limit support pressure and the boundary of the yielded zone.

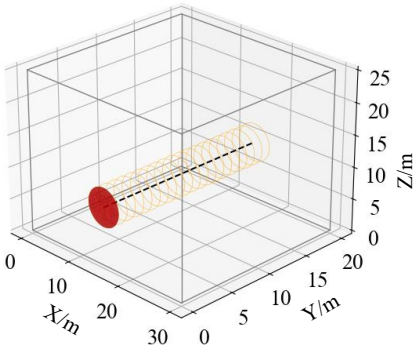


Fig. 7 Numerical model

3.3 Identification of Failure Modes and Critical Cover-to-Diameter Ratio

To eliminate the effects of tunnel size and soil unit weight on the limit support pressure and facilitate

comparison among different cases, the limit support pressure coefficient is introduced as:

$$N_\gamma = \frac{p_{\lim}}{\gamma_{\mathrm{ref}} D} \tag{4}$$

where N_γ is the limit support pressure coefficient, $p_{\lim}$ is the limit support pressure, γ_{ref} is the reference soil unit weight (corresponding to the unit weight of the upper sand layer), and D is the tunnel diameter. A larger N_γ indicates a higher support pressure required to maintain tunnel-face stability.

To determine whether the soil has reached the yield state and to identify the potential failure zone, the yield residual stress is introduced as:

$$\sigma_c = -f(\sigma) \tag{5}$$

where σ_c is the yield residual stress and $f(\sigma)$ is the Mohr–Coulomb yield function. When $\sigma_c>0$, the soil remains below the yield state; when σ_c approaches zero, the soil reaches the yield state. The failure mode and critical cover-to-diameter ratio can therefore be identified according to the distribution and connectivity of the near-zero-σ_c regions. For comparison among different cases, the yield residual stress was normalized as $\sigma_c=\gamma_{\mathrm{ref}}D$, where values approaching zero indicate that the soil approaches the yield state.

Elements in which the Mohr–Coulomb yield constraint approaches or reaches the active state are regarded as the potential yielded zone. If the yielded zone is confined to the vicinity of the tunnel face and closes within the soil mass, the failure mode is classified as local failure. In contrast, if the yielded zone continuously propagates upward and forward from the tunnel face and extends to the ground surface, the failure mode is classified as global failure. The value of C/D corresponding to the transition from global failure to local failure is defined as the critical cover-to-diameter ratio.

3.4 Model Validation and Analysis

To evaluate the reliability of the three-dimensional lower-bound numerical model, the limit support pressures obtained for different test cases were compared with the centrifuge test results. As shown in Table 6, the upper sand layer reached the limit state first in both D1 and D2, and the limit support pressure of D2 was slightly higher than that of D1. No failure occurred in cases D3 and D4.

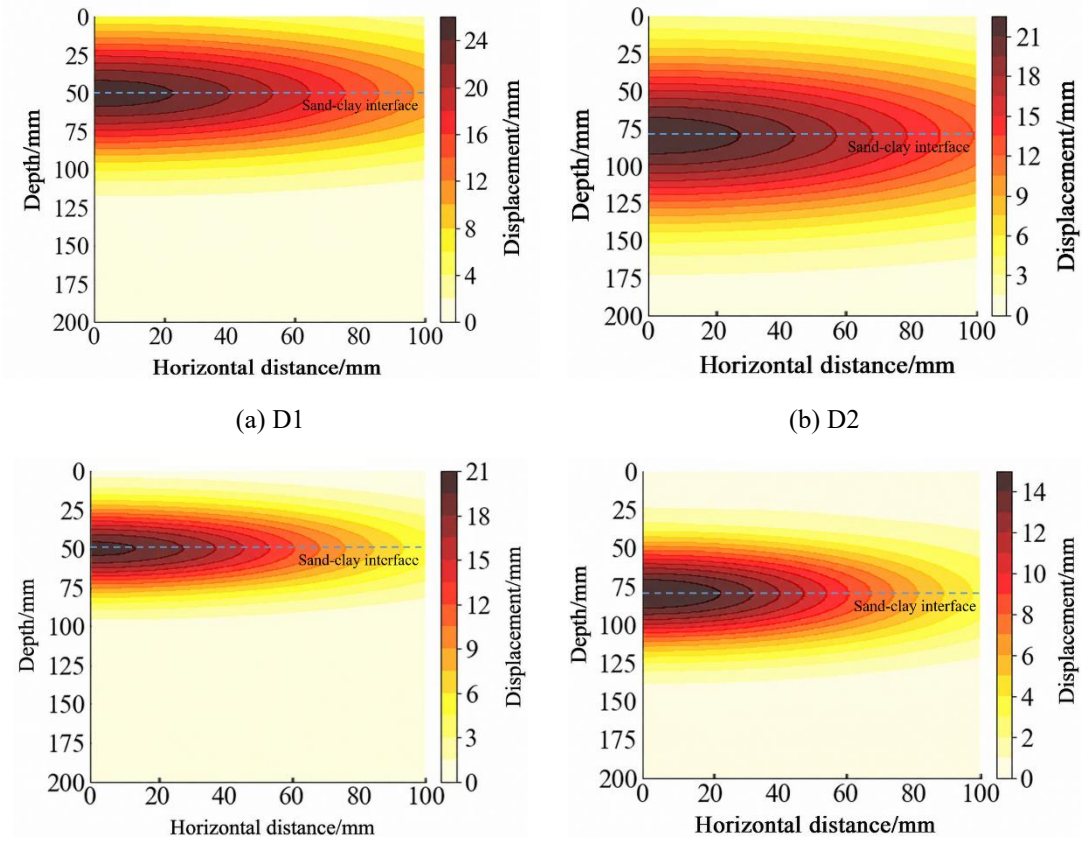
Table 6 Comparison of limit support pressures obtained from numerical analysis and centrifuge tests

Case	Centrifuge test $P_{\min}$ / kPa	Numerical analysis $P_{\min}$ / kPa	Deviation / %
D1	12.7	11.5	−9.4
D2	13.4	12.8	−4.5
D3	No limit state reached	5.3	—
D4	No limit state reached	6.3	—

The deviations between the numerical and experimental results for D1 and D2 were −9.4% and −4.5%, respectively, both within 10%. Moreover, both the numerical analysis and centrifuge tests showed that the limit support pressure of D2 was higher than that of D1. The numerical values were slightly lower than the experimental results, which is consistent with the theoretical characteristics of lower-bound solutions [16]. For cases D3 and D4, no limit state was reached within the prescribed face retraction range of the centrifuge tests. The lower-bound analysis nevertheless yielded finite limit support pressures, which were substantially lower than those of D1 and D2, indicating the stabilizing effect of the clay layer when the soil-layer interface was located at the tunnel crown. These results indicate that the proposed model can predict the limit support pressure of the tunnel face with satisfactory accuracy.

Figure 8 presents the horizontal displacement contours of the failure zones obtained from the numerical analysis. For cases D1 and D2, the numerically predicted failure zones propagated upward and

outward from the tunnel face and extended to the ground surface. Their initiation positions, propagation directions, and overall profiles were generally consistent with the experimental observations, indicating that the numerical model can effectively reproduce the global failure characteristics governed by the upper sand layer.



(a) D1 (b) D2

(c) D3 (d) D4

Fig. 8 Horizontal displacement contours ahead of the tunnel face obtained from numerical analysis

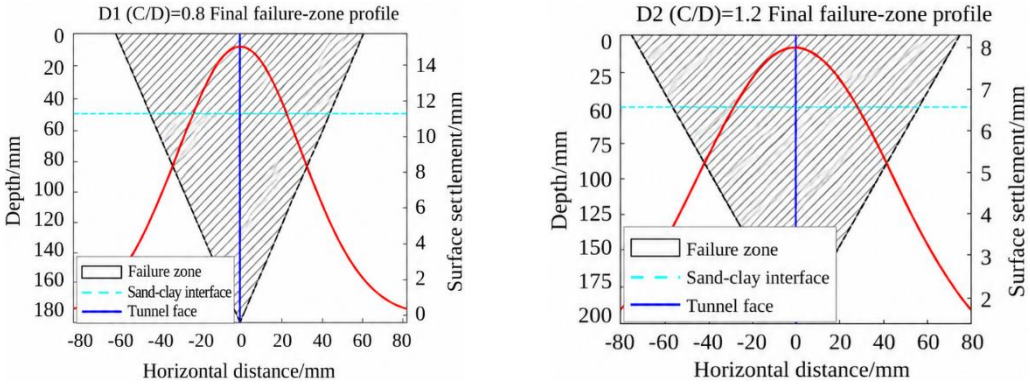
4 Numerical Simulation and Parametric Analysis

4.1 Failure Patterns

As shown in Fig. 8, when the soil-layer interface intersected the center of the tunnel face (D1 and D2), the maximum horizontal displacement was concentrated in the middle and upper portions of the sand layer, and the displacement contours propagated asymmetrically upward. In case D1 (C/D=0.8), the failure zone extended to the ground surface, whereas in case D2 (C/D=1.2), the displacement extended over a wider region at greater depths. Only minor displacements occurred within the clay layer, indicating that the underlying clay effectively restricted the downward propagation of the failure zone. When the soil-layer interface was raised to the tunnel crown (D3 and D4), the displacement was confined to within approximately 1.5 tunnel diameters ahead of the face and did not propagate upward. Moreover, the maximum displacement was approximately 60% lower than that in D1. These results indicate that the thickness of the clay layer is a key factor controlling the failure mode. When the soil-layer interface is located at or above the tunnel crown, the clay layer can effectively inhibit the upward propagation of the failure zone.

A comparison of the experimentally observed failure-zone profiles and surface settlement troughs (Fig. 4) with the numerical results (Fig. 9) for cases D1 and D2 shows that the failure zone in D1 exhibited a narrow upper portion and a wider lower portion, with its upper boundary extending to the ground

surface. The surface settlement trough showed a relatively high and narrow single-peak profile, with a maximum settlement of approximately 15 mm directly above the tunnel centerline. Furthermore, almost the entire sand layer above the sand–clay interface was involved in the failure zone. In case D2, the failure zone was more extensive, whereas the surface settlement trough was noticeably broader and flatter, with a maximum settlement of approximately 8 mm. The lower portion of the sand layer remained relatively intact under this condition.



(a) D1 (b) D2

Fig. 9 Final failure-zone profiles and surface settlement troughs at different cover-to-diameter ratios

4.2 Analysis of the Critical Cover-to-Diameter Ratio

To investigate the combined effects of cover depth and soil shear strength on the tunnel-face failure mode, the soil-layer interface was maintained at the center of the tunnel face, while the soil unit weight, cohesion, and parameters of the lower clay layer were kept constant. Only the internal friction angle ϕ of the upper sand layer was varied. The values of ϕ were set to 15°, 20°, 25°, 30°, and 35°, while C/D ranged from 0.50 to 2.50. Near the transition between global and local failure, C/D was refined at an interval of 0.10 to determine the critical cover-to-diameter ratio.

Figure 10 shows the variation in N_γ with C/D for different internal friction angles. As the cover-to-diameter ratio increased, N_γ initially increased and subsequently tended to stabilize for all values of ϕ. At relatively small C/D, the potential failure zone readily propagated upward to the ground surface, and the limit support pressure was strongly affected by the overlying soil and the ground-surface boundary. With increasing C/D, the potential failure zone gradually became confined ahead of the tunnel face, reducing the influence of the ground-surface boundary. Consequently, the increase in N_γ gradually diminished until the coefficient approached a stable value.

At the same cover-to-diameter ratio, N_γ decreased with increasing internal friction angle. At C/D=1.50, for example, N_γ decreased from 0.108 to 0.056 as ϕ increased from 15° to 35°, corresponding to a reduction of approximately 48.1%. Moreover, the variation in N_γ with increasing C/D became less pronounced at larger internal friction angles. This indicates that an increase in the shear strength of the sand layer can reduce the support pressure required to maintain tunnel-face stability and decrease its sensitivity to variations in cover depth.

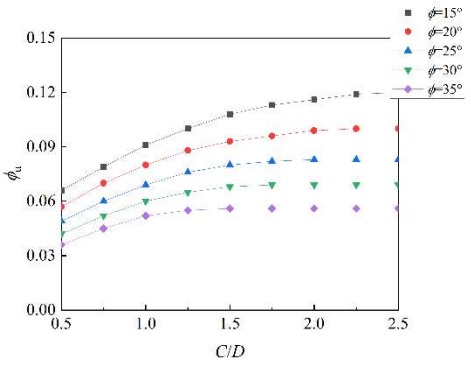


Fig. 10 Variation in the limit support pressure coefficient with cover-to-diameter ratio for different internal friction angles

The distribution of the yield residual stress and the variation trend of the N_γ curves were used as criteria for determining the critical cover-to-diameter ratio. When the near-zero-σ_c region continuously extended from the tunnel face to the ground surface, the tunnel face exhibited global failure. When this region was no longer connected to the ground surface and instead became confined ahead of the tunnel face, the failure mode changed to local failure. For a given internal friction angle, the minimum C/D at which the failure mode changed from global to local failure was defined as the critical cover-to-diameter ratio, $(C/D)_{crit}$.

Figure 11 shows the distributions of yield residual stress immediately below and above the critical cover-to-diameter ratio for different internal friction angles. When C/D<$(C/D)_{crit}$, the near-zero-σ_c region propagated upward from the tunnel face and reached the ground surface, resulting in a relatively extensive potential failure zone and global failure. When C/D≥$(C/D)_{crit}$, the near-zero-σ_c region was mainly concentrated and enclosed ahead of the tunnel face, indicating a transition to local failure. The cover-to-diameter ratio at which the potential failure zone changed from a surface-reaching pattern to a locally confined pattern was generally consistent with the position at which the N_γ curve approached a stable value.

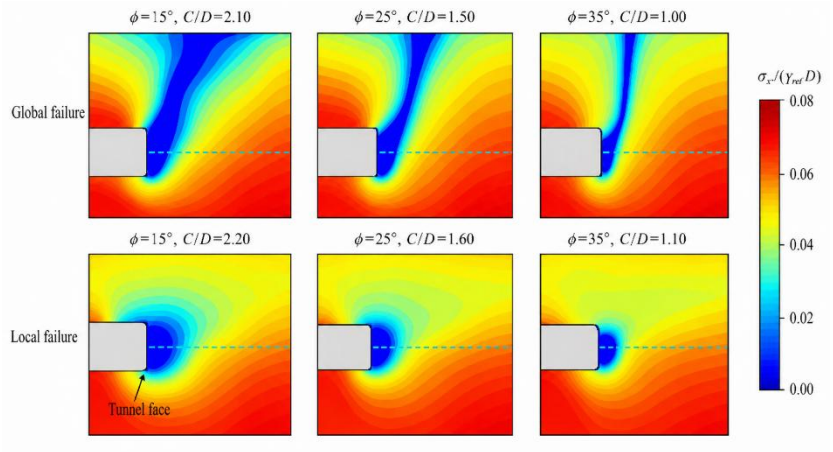


Fig. 11 Yield residual stress distributions below and above the critical cover-to-diameter ratio for different internal friction angles (representative internal friction angles)

The critical cover-to-diameter ratios obtained for different internal friction angles are summarized in Table 7.

Table 7 Critical cover-to-diameter ratios for different internal friction angles

ϕ / °	$(C/D)_{global}$	$(C/D)_{local}$	$(C/D)_{crit}$	Critical N_γ
15	2.1	2.2	2.2	0.118
20	1.8	1.9	1.9	0.098
25	1.5	1.6	1.6	0.081
30	1.2	1.3	1.3	0.067
35	1.0	1.1	1.1	0.054

In Table 7, $(C/D)_{global}$ denotes the maximum cover-to-diameter ratio corresponding to global failure, while $(C/D)_{local}$ denotes the minimum cover-to-diameter ratio corresponding to local failure.

As shown in Table 7, when the internal friction angle increased from 15° to 35°, the critical cover-to-diameter ratio decreased from 2.20 to 1.10, representing a reduction of 50.0%. Meanwhile, the limit support pressure coefficient at the critical condition decreased from 0.118 to 0.054, corresponding to a reduction of approximately 54.2%. These results indicate that increasing the internal friction angle not only reduces the limit support pressure required at the tunnel face but also enables the potential failure zone to become confined ahead of the tunnel face at a smaller cover-to-diameter ratio.

A linear regression was performed to establish the relationship between the critical cover-to-diameter ratio and the internal friction angle (empirical linear regression within $15°\leq\phi\leq35°$):

$$(C/D)_{crit} = 3.02 - 0.056\phi \tag{6}$$

The coefficient of determination was R^2=0.995, indicating that, within the parameter range considered in this study, the critical cover-to-diameter ratio decreased approximately linearly with increasing internal friction angle of the upper sand layer. As shown in Fig. 12, the region below the critical line corresponds to global failure, whereas the region above the critical line corresponds to local failure:

$$\begin{aligned} C/D &< (C/D)_{crit} \quad \text{global failure} \\ C/D &\geq (C/D)_{crit} \quad \text{local failure} \end{aligned} \tag{7}$$

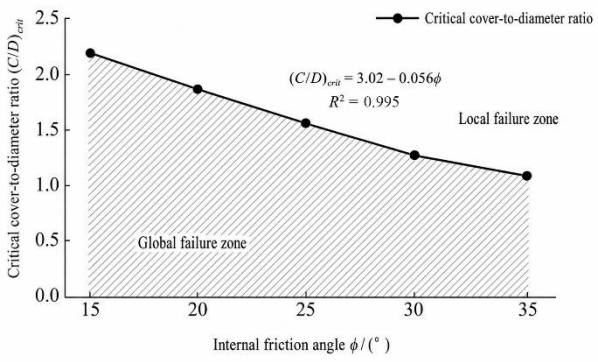


Fig. 12 Variation in the critical cover-to-diameter ratio with internal friction angle

As the internal friction angle increased, the shear strength and soil-arching effect of the upper sand layer were enhanced, allowing a more stable load-transfer mechanism to develop above the tunnel face. This restricted the propagation of the potential failure zone toward the ground surface and enabled the failure mode to transition from global to local failure at a smaller cover-to-diameter ratio. Conversely, shallow ground with a low internal friction angle was more susceptible to the influence of the ground-surface boundary and exhibited a larger potential failure zone; therefore, greater attention should be paid to tunnel-face support and surface deformation control during construction. Once the cover-to-diameter

ratio exceeded the critical value, further increases in cover depth had progressively less influence on the limit support pressure and the extent of the potential failure zone.

5 Conclusions

Based on the centrifuge model tests, PIV image analysis, and three-dimensional lower-bound finite-element limit analysis, the following main conclusions were drawn.

(1) The position of the soil-layer interface is a key factor controlling the tunnel-face failure mode. When the interface intersected the center of the tunnel face, failure occurred predominantly in the upper sand layer and propagated upward and outward from the face. When the interface was located at the tunnel crown, the lower clay layer effectively restricted the development of the failure zone, and no continuous failure zone formed in cases D3 and D4 within the prescribed face retraction displacement of 30 mm.

(2) Tunnel-face failure exhibited a distinct progressive evolution and could be divided into three stages: local deformation, progressive failure, and residual stability. Both earth-pressure release and support-stress reduction were considerably more pronounced in the sand layer than in the clay layer. Cases D1 and D2 reached the limit state at a face retraction displacement of approximately 10 mm, with corresponding limit support pressures of 12.7 kPa and 13.4 kPa, respectively.

(3) As the cover-to-diameter ratio increased from 0.8 to 1.2, the horizontal and deep extents of the failure zone increased, whereas the peak surface settlement decreased from approximately 15 mm to 8 mm. The limit support pressure increased by only about 5.5%, indicating that the effect of increasing C/D from 0.8 to 1.2 on the limit support pressure was relatively limited under the investigated soil-layer configuration.

(4) The deviations between the limit support pressures obtained from the three-dimensional lower-bound analysis and the centrifuge test results were both within 10%, and the predicted failure-zone patterns were generally consistent with the experimental observations. As the internal friction angle of the upper sand layer increased from 15° to 35°, the critical cover-to-diameter ratio decreased from 2.20 to 1.10, indicating that the increase in sand shear strength promoted closure of the failure zone ahead of the tunnel face and facilitated the transition from global failure to local failure.

Declarations

Author Contributions: Conceptualization, Kun Yang and Jian Xu; methodology, Kun Yang, Jian Xu and Bolin Jiang; investigation, Kun Yang, Chen Tang and Weitong He; data curation, Kun Yang and Chen Tang; formal analysis, Kun Yang and Bolin Jiang; writing—original draft preparation, Kun Yang; writing—review and editing, Jian Xu, Bolin Jiang, Chen Tang and Weitong He; supervision, Jian Xu; project administration, Jian Xu. All authors have read and agreed to the published version of the manuscript.

Funding: This research was supported by the Science and Technology Research Program of Chongqing Municipal Education Commission (Grant No.KJZD-K202503402, KJZD-M202603401).

Data Availability Statement: The data that support the findings of this study are available from the corresponding author upon reasonable request.

Conflicts of Interest: The authors declare no conflicts of interest.

Ethical approval

Not applicable

Consent to participate

The authors declare that they have no known competing financial interests or personal relationships that

could have appeared to influence the work reported in this paper.

Consent to publish

Not applicable

Clinical trial

Not applicable

References:

[1] Kirsch A. Experimental investigation of the face stability of shallow tunnels in sand. Acta Geotech. 2010;5(1):43–62. https://doi.org/10.1007/s11440-010-0110-7

[2] Chen RP, Li J, Kong LG, Tang LJ. Experimental study on face instability of shield tunnel in sand. Tunn Undergr Space Technol. 2013;33:12–21. https://doi.org/10.1016/j.tust.2012.08.001

[3] Liu W, Zhao Y, Shi PX, Li JY, Gan PL. Face stability analysis of shield-driven tunnels shallowly buried in dry sand using 1-g large-scale model tests. Acta Geotech. 2018;13(3):693–705. https://doi.org/10.1007/s11440-017-0607-4

[4] Lü XL, Zhou YC, Huang MS, Zeng S. Experimental study of the face stability of shield tunnel in sands under seepage condition. Tunn Undergr Space Technol. 2018;74:195–205. https://doi.org/10.1016/j.tust.2018.01.015

[5] Weng XL, Sun YF, Yan BH, Niu HS, Lin RA, Zhou SQ. Centrifuge testing and numerical modeling of tunnel face stability considering longitudinal slope angle and steady state seepage in soft clay. Tunn Undergr Space Technol. 2020;101:103406. https://doi.org/10.1016/j.tust.2020.103406

[6] Berthoz N, Branque D, Subrin D, Wong H, Humbert E. Face failure in homogeneous and stratified soft ground: theoretical and experimental approaches on 1g EPBS reduced scale model. Tunn Undergr Space Technol. 2012;30:25–37. https://doi.org/10.1016/j.tust.2012.01.005

[7] Alagha ASN, Chapman DN. Numerical modelling of tunnel face stability in homogeneous and layered soft ground. Tunn Undergr Space Technol. 2019;94:103096. https://doi.org/10.1016/j.tust.2019.103096

[8] Ibrahim E, Soubra AH, Mollon G, Raphael W, Dias D, Reda A. Three-dimensional face stability analysis of pressurized tunnels driven in a multilayered purely frictional medium. Tunn Undergr Space Technol. 2015;49:18–34. https://doi.org/10.1016/j.tust.2015.04.001

[9] Senent S, Jimenez R. A tunnel face failure mechanism for layered ground, considering the possibility of partial collapse. Tunn Undergr Space Technol. 2015;47:182–192. https://doi.org/10.1016/j.tust.2014.12.014

[10] Han KH, Zhang CP, Zhang DL. Upper-bound solutions for the face stability of a shield tunnel in multilayered cohesive-frictional soils. Comput Geotech. 2016;79:1–9. https://doi.org/10.1016/j.compgeo.2016.05.018

[11] Ma SK, Duan ZB, Huang Z, Liu Y, Shao Y. Study on the stability of shield tunnel face in clay and clay-gravel stratum through large-scale physical model tests with transparent soil. Tunn Undergr Space Technol. 2022;119:104199. https://doi.org/10.1016/j.tust.2021.104199

[12] Tu SQ, Li W, Zhang CP, Chen W. Effect of inclined layered soils on face stability in shield tunneling based on limit analysis. Tunn Undergr Space Technol. 2023;131:104773. https://doi.org/10.1016/j.tust.2022.104773

[13] Li X, Weng X, Ye F, Dang B, Zhang X, Sun Y, Li N. Face stability of shallow shield tunnels in inclined sand-clay strata: effects of dip angle and interface elevation. Tunn Undergr Space Technol. 2026;173:107651. https://doi.org/10.1016/j.tust.2026.107651

[14] Fernández F, Rojas JEG, Vargas EA Jr, Velloso RQ, Dias D. Three-dimensional face stability analysis of shallow tunnels using numerical limit analysis and material point method. Tunn Undergr Space Technol. 2021;112:103904. https://doi.org/10.1016/j.tust.2021.103904

[15] Krabbenhøft K, Lyamin AV, Sloan SW. Three-dimensional Mohr–Coulomb limit analysis using semidefinite programming. Commun Numer Methods Eng. 2008;24(11):1107–1119. doi:10.1002/cnm.1018.

[16] Kumar J, Mohapatra D. Lower-bound finite elements limit analysis for Hoek–Brown materials using semidefinite programming. J Eng Mech. 2017;143(9):04017077. doi:10.1061/(ASCE)EM.1943-7889.0001296.